Catalysis Science & Technology

ROYAL SOCIETY OF CHEMISTRY

PAPER

View Article Online
View Journal | View Issue

Cite this: *Catal. Sci. Technol.*, 2021, **11**, 1780

Selective catalytic reduction of NO with NH_3 over Cu-exchanged CHA, GME, and AFX zeolites: a density functional theory study†

Pei Zhao, *[ab] Bundet Boekfa,[c] Ken-ichi Shimizu, [bd] Masaru Ogura [be] and Masahiro Ehara *[ab]

Density functional theory calculations have been applied to study the selective catalytic reduction of NO by NH_3 over the Cu-exchanged zeolites with *cha*, *gme*, and *aft* cages. The Cu^{I}, Cu^{II}, and $[Cu^{II}(OH)]^+$ ions are considered as the active sites to study both the reduction and oxidation processes during the catalytic cycle. In the case of the reduction process, the NH_2NO formation at the $[Cu^{II}(OH)]^+$ site possesses high barriers in the three frameworks, while the lower barriers are found at the Cu^{II} site. Importantly, it is found that the barriers are largely decreased at the solvated $[Cu^{II}(NH_3)_4]^{2+}$ site for the *cha* and *aft* frameworks, while the barrier is only slightly decreased for the *gme* cage. As for the oxidation, the nitrate formation has similar reaction barriers at the Cu^{I} site of the three frameworks, which are lower than the following nitrite formation. In particular, the smallest *gme* cage possesses the highest barrier for the nitrite formation. Calculations on the O_2 activation by the NH_3-solvated Cu dimer revealed that the *cha* and *aft* cages have better performance than the *gme* cage, and the much smaller adsorption energy of O_2 in the *gme* cage indicates the unfavorable O_2 insertion. Therefore, the selectivity caused by the cage size is identified during the reaction process, and the *cha* and *aft* cages are more favorable.

Received 4th December 2020,
Accepted 4th January 2021

DOI: 10.1039/d0cy02342f

rsc.li/catalysis

[a] *Research Center for Computational Science, Institute for Molecular Science, Okazaki, 444-8585, Japan*
[b] *Element Strategy Initiative for Catalysts and Batteries (ESICB), Kyoto University, Kyoto 615-8245, Japan. E-mail: pei@ims.ac.jp, ehara@ims.ac.jp*
[c] *Department of Chemistry, Faculty of Liberal Arts and Science, Kasetsart University, Kamphaengsaen Campus, Nakhonpathom 73140, Thailand*
[d] *Institute for Catalysis, Hokkaido University, Sapporo 001-0021, Japan*
[e] *Institute of Industrial Science, The University of Tokyo, Tokyo 153-8505, Japan*

† Electronic supplementary information (ESI) available: The computational models of *cha* (42T), *gme* (36T) and *aft* (54T); the reaction mechanism for the SCR reaction in the Cu-zeolite; reaction energy diagrams and optimized structures of intermediates and transition states for reduction by NO and NH_3 on Cu^{II}OH–Al-*cha* and Cu^{II}OH–Al-*aft*; reaction energy diagrams and optimized structures of intermediates and transition states for reduction by NO and NH_3 on Cu^{II}–2Al-*gme* and -*aft*; deformation energies of intermediates and transition states with respect to the pristine structures of Cu^{II}–2Al-*cha*, -*gme*, and -*aft*; reaction energy diagrams and local structures of intermediates and transition states for oxidation by Cu^{I}–2AlH-*cha*, -*gme*, and -*aft*; local geometries of the INT1, TS1, INT2, TS2 and INT3 of *cha*, *gme*, and *aft* at the 2Al site; local geometries of the TS3, INT5, and INT6 of *cha*, *gme*, and *aft* at the Al site; deformation energies of intermediates and transition states for the oxidation with respect to the pristine structures of Cu^{I}-Al-*cha*, -*gme*, and -*aft*; deformation energies of intermediates and transition states for the oxidation with respect to the pristine structures of Cu^{I}–2AlH-*cha*, -*gme*, and -*aft*; optimized structures and relative energies of INT1, INT2, and INT4 for *gme* and *aft*; interaction energies between the $[zeolite]^{2-}$ cage and the inner $2[Cu^{I}(NH_3)_2]^+/2[OCu^{I}(NH_3)_2]^+$ ion in INT1 and INT4 as well as relative energies of the outer cage and the inner ion for *cha* and *aft*; local geometries of intermediates and transition states for the O_2 activation by the $2[NH_3$-Cu^{I}-$NH_3]$ dimer in 2Al-*gme*, and -*aft*; potential energy surface between INT2 and INT3 for the O_2 activation by the $2[NH_3$–Cu^{I}–$NH_3]$ dimer in 2Al-*cha*; natural electron configuration of Cu in Cu-*cha*, Cu-*gme*, and Cu-*aft*; NPA charge of Cu in Cu-*cha*, Cu-*gme*, and Cu-*aft*. See DOI: 10.1039/d0cy02342f

Introduction

Zeolites are inorganic microporous crystalline materials constructed of corner-sharing SiO_4 and AlO_4 tetrahedra, or other TO_4 sites (oxygen atoms bridge the tetrahedral atoms).[1] The generation of a negative charge, when Si^{4+} is substituted by Al^{3+} in the oxide framework, dictates the need for a balancing cation. This exchange capacity can lead to Cu-exchanged zeolites that are active for the selective catalytic reduction (SCR) of NO to N_2 by ammonia (NH_3-SCR).[2,3] The small-pore Cu-exchanged CHA zeolites, in particular SSZ-13 and SAPO-34, have attracted much attention due to their high activity and hydrothermal stability.[4–8] The simple structure of the Cu-CHA zeolite is also important for the fundamental SCR investigations. As for the standard SCR reaction ($4NH_3 + 4NO + O_2 \rightarrow 4N_2 + 6H_2O$) on Cu-CHA, lots of mechanistic studies have revealed that (1) the reaction follows a redox reaction mechanism by the Cu-ion cycle between +2 and +1 oxidation states and (2) the isolated Cu ions (Cu^{II} and $[Cu^{II}(OH)]^+$) act as the active centers.[9–17]

The small-pore CHA zeolites have the largest openings of 8-membered rings (*8r*), which excels in applications dealing with smaller molecules and ions.[7] Reactants and products penetrate through micropores of zeolites, which can control the selectivity accordingly. Meanwhile, the formed cages or larger intersections in the zeolite framework can influence the formed intermediates during the reaction process, which

eventually results in differences in the catalytic activity. As shown in Fig. 1a, the double six-membered-ring (*d6r*) layers are stacked in an ABC sequence, forming the *cha* cage interconnected by *8r* windows.[18] The small-pore zeolite AFX is formed by two types of cages, *gme* and *aft*, which have the stackings of the same *d6r* layers in the BC and ABCB sequences, respectively (Fig. 1b).[19] The *cha*, *gme*, and *aft* cages share the same *4r*, *d6r*, and *8r* pores, but with a different cavity size (*aft* > *cha* > *gme*). Recently, the Cu-exchanged AFX zeolites have been proven to be effective catalysts for NH_3-SCR reactions, which are also hydrothermally stable.[20–23] In the case of NH_3-SCR on a Cu-CHA zeolite, it has been shown that the active Cu ions are located in the *6r* and *8r* of the framework,[24–26] however, the Cu ions are lifted out from their original positions into the large cavities upon the adsorption of NH_3, NO, or other ligands.[27,28] Therefore, the SCR reaction actually takes place in the large cavities, especially for the NH_3-solvated Cu ions.[16,29] It has been reported that the Cu ions are detached from the zeolite structure into the pore under the exposure of NH_3 below 250 °C.[16,30–32] Cu^I can be solvated by two NH_3 ligands forming a linear $[Cu^I(NH_3)_2]^+$ complex, and Cu^{II} can form the fourfold coordinated complex of $[Cu^{II}(NH_3)_4]^{2+}$.[33,34] Meanwhile, at low Cu loadings, the observed quadratic dependence on the Cu loading indicates the reaction involves two Cu sites at low temperatures, which has been attributed to the activation of oxygen by paring of $[Cu^I(NH_3)_2]^+$.[16,29,35] So far, the related studies are mainly focused on the CHA zeolites, and the role of cavity in different small-pore zeolites remains to be studied for the NH_3-SCR reaction.

In this paper, we aim to unravel the impact of the cavity size on the SCR performance in the *cha*, *gme*, and *aft* cages by density functional theory (DFT) calculations. The Cu ions in zeolites show different ammonia SCR activities depending on the Cu environmental structure (cage and local Al number), which has led to numerous studies experimentally. Nevertheless, the activity evaluation on the Cu ions in various cages is inaccessible due to multiple environments of active Cu ions, making theoretical calculations an ideal method for the related studies. As summarized in Scheme S1,† the oxidation and reduction half-cycles of the SCR reaction are both studied, and they take place at NO + O_2 and NH_3 + NO atmospheres, respectively. The Cu^I ion or the $Cu^{II}/[Cu^{II}(OH)]^+$ species acts as the active sites, which anchor at zeolite frameworks. The small *gme* cages in the large pore GME zeolites are considered to be the active Cu-ion sites for SCR reaction, which also makes our study useful for the GME zeolites. The ammonia-solvated Cu cations are also taken into account to study the NH_2NO formation and the O_2 activation. This work will provide a further understanding of the catalytic activity of the Cu-exchanged zeolites with *cha*, *gme*, and *aft* cages.

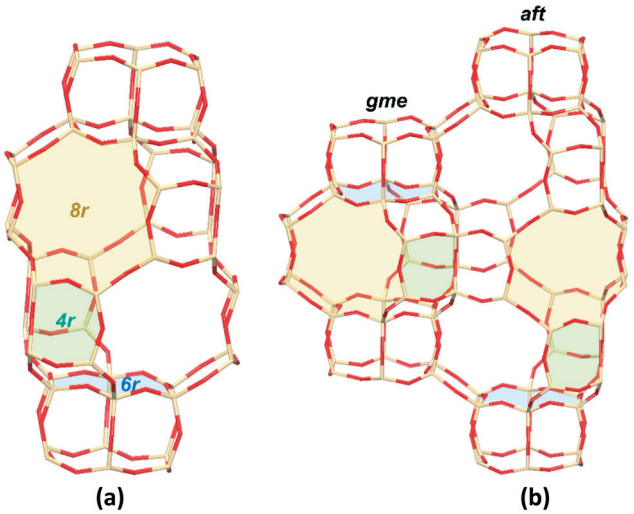

Fig. 1 Schematic representations of CHA (a) and AFX (b) topologies. The green, blue, and yellow filled areas stand for the 4-, 6-, and 8-membered rings, respectively (color code: Si tan; O red).

Computational details

Computational models

The 42T, 36T, and 54T clusters are applied for the *cha*, *gme*, and *aft* frameworks in our calculations (T represents the tetrahedrally coordinated Si or Al atoms), as shown in Fig. S1.† The computational models with one/two aluminum sites are both considered in our calculations to evaluate the effect of the Al content. We considered the Al atoms only have the charge-compensating effect on the Cu atom which is hosted in the same unit as the Al atoms.[24] DFT calculations have generally indicated that the isolated Cu^I and Cu^{II} ions prefer the *d6r* site of the *cha* framework.[11,12,24,36–40] Meanwhile, the two Al atoms are distributed in an AlSiSiAl configuration, which is the most favorable structure when placing both Al atoms and the Cu^{II} cation within the same *d6r*.[38] Fig. 2 shows the constructed structures with one/two aluminum sites. Due to the similar topologies, the *gme* and *aft* frameworks exhibit the same preference for the *d6r* site. When the OH^- ligand is coordinated to the Cu^{II} ion, the preference for the *d6r* site diminishes, which accords with the previous reports.[13,41] The $[Cu^{II}(OH)]^+$ in the *d6r* is 3 kJ mol^{-1} lower in energy than that in the *8r* site for the *gme* cage, while the *cha* and *aft* cages both have slightly lower energies in the *8r* than the *d6r*. As for the structures with two Al atoms, the Cu^I ion is accompanied by a Brønsted proton in the framework. The computational models including the cuprous ion were used for the oxidation process, while those including the cupric ion were used for the reduction process. The zeolite cages have two Al atoms when the NH_3-solvated Cu ions ($[Cu^{II}(NH_3)_4]^{2+}$ and $[Cu^I(NH_3)_2]^{2+}$) act as the active site.

Computational methods

The calculations were carried out using the M06-L density functional.[42] The M06-L method is reliable for the adsorption and activation energy studies on zeolites.[43–46] The 6-31G (d,

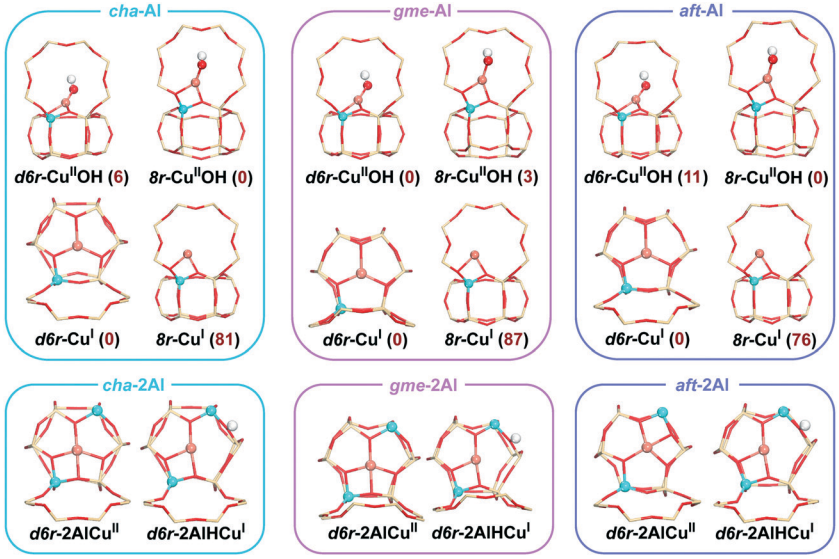

Fig. 2 Local geometries of Cu^{I}, $[Cu^{II}(OH)]^{+}$, and Cu^{II} in the *d6r* and *8r* of *cha*, *gme*, and *aft* cages. Values in parenthesis are relative energies (in kJ mol^{-1}) (color code: Al light blue; Si tan; Cu rufous; O red; H white).

p) basis set was applied for the Al, Si, O, N and H atoms,[47,48] and the Stuttgart effective core potential (ECP) basis set was adopted for the Cu atom.[49] Only the terminal hydrogen atoms were kept fixed with X-ray structure while other atoms were allowed to relax. Based on the optimized structures, vibrational analyses were conducted to verify the stationary points to be minima or saddle points on the potential energy surface. All DFT calculations were conducted using Gaussian 09 suite of programs version E.01.[50] Natural population analyses on all the structures were performed using NBO 3.1 as implemented in Gaussian 09.

Results and discussion

SCR reaction cycles

As shown in Scheme S1,† the reduction of Al–Cu^{II}OH and the oxidation of Al–Cu^{I} constitute the catalytic cycle on the 1Al site,[13,21] while the reduction of 2Al–Cu^{II} and the oxidation of 2AlH–Cu^{I} form the catalytic cycle on the 2Al site.[12,14] As for the reduction process, the adsorption of NO and NH_3 at $[Cu^{II}$-$OH]^{+}$ gives the NOOH–Cu^{I}–NH_3 species, which generates a water molecule followed by the formation of Cu^{I}–NH_2NO. The adsorption of NO and NH_3 to the Cu^{II} on the 2Al site results in the formation of Cu^{I}–NH_2NO by the N–H dissociation of NH_3, and the H atom is transferred to the framework forming a Brønsted acid site. The Cu^{I}–NH_2NO species then gives the N_2 and H_2O molecules. The oxidation takes place in the presence of NO and O_2. The Cu^{I} ion reacts with NO and O_2 to form the nitrate species, and the nitrite species is formed after the adsorption of the second NO molecule. The same nitrate and nitrite species exist on the 1Al and 2Al sites. Subsequently, the adsorption of NH_3 leads to the NO_2^{-}–Cu^{II}–NH_3 species on 1Al and the NO_2^{-}–Cu^{II}–NH_4^{+} species on 2Al, which eventually can generate N_2 and H_2O.

Reduction in Cu-*cha*, Cu-*gme*, and Cu-*aft*

Previous studies have proven that the presence of NO and NH_3 can effectively reduce the Cu^{II} ion,[6] so the NO and NH_3 molecules are co-adsorbed on the Cu ion in our calculations. The reaction pathways of reduction are first studied based on Cu^{II}OH-*cha*, -*gme*, and -*aft*, where the $[Cu^{II}(OH)]^{+}$ unit is the active site. In this case, one ammonia molecule is adsorbed, and the $[Cu^{II}(OH)]^{+}$ unit is placed at the *8r* site due to the preferred stability. The reaction pathway involving NO and an NH_3 molecule at the $[Cu^{II}(OH)]^{+}$ site has been proposed for the *cha* framework, however, the detailed information such as the energy barrier is still absent.[13,21,51]

All energies shown in these diagrams are measured with respect to the isolated zeolites and the NO/NH_3 molecule. Spin multiplicities of intermediates and transition states are shown in Fig. S11–S13.† The adsorption of NO and NH_3 is exothermic with adsorption energies of −225, −236, and −230 kJ mol^{-1} for *cha*, *gme*, and *aft*, as shown in Fig. 3 and S2.† Subsequently, the Cu–O bond is lengthening, the Cu^{I}–NOOH species is formed through energy barriers of 38, 32, and 47 kJ mol^{-1} for *cha*, *gme*, and *aft*, and the resulting species is similar to the proposed Cu^{I}–NO^{+} species.[52,53] The formation of the Cu^{I}–NOOH species is slightly exothermic relative to the NO^{+}–Cu^{I}–OH^{-} species, which is the same as the previous report.[51] The energy barriers for the H_2O formation are 131, 147, and 153 kJ mol^{-1} for *cha*, *gme*, and *aft*. The following desorption of H_2O is endothermic, which exhibits the same reaction energy of −48 kJ mol^{-1} for the three frameworks. After low energy barriers of 10, 11, and 12 kJ mol^{-1} for *cha*, *gme*, and *aft*, the N–N bond formation leads to NH_2NO, which is an exothermic step. At this step, two possible intermediates of INT5 and INT5′ are located. In the case of INT5′, one N atom of the NH_2NO is coordinated to the Cu atom, while the two N atoms of NH_2NO are coordinated to

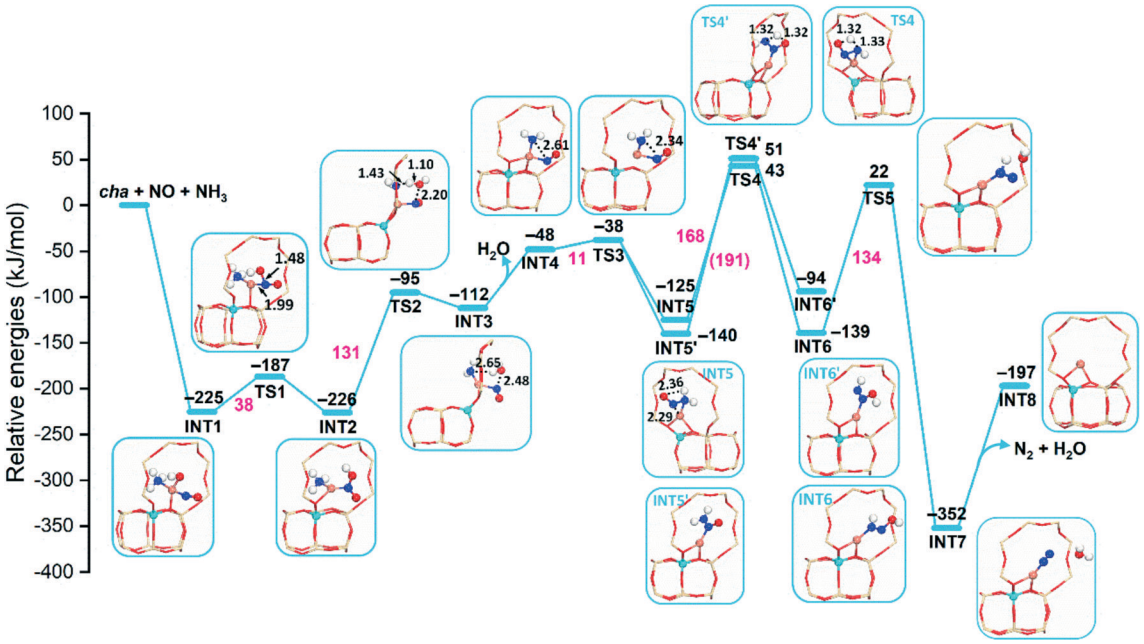

Fig. 3 Reaction energy diagrams and optimized structures of intermediates and transition states for reduction by NO and NH_3 on $Cu^{II}OH$–Al-*cha*. The values of energetics and energy barriers are shown in black and magenta, respectively (color code: Al light blue; Si tan; Cu rufous; N mazarine; O red; H white).

the Cu atom in INT5. INT5′ is more stable than the INT5 for the three frameworks.

In the case of *cha* and *aft*, the following energy barriers for the H transfer from INT5 (168 and 164 kJ mol^{-1} for *cha* and *aft*) are lower than those from INT5′ (191 and 196 kJ mol^{-1} for *cha* and *aft*). As for the *gme* cage, two close energy barriers are identified, that is, 152 and 156 kJ mol^{-1} from INT5′ and INT5, which are lower than those on the *cha* and *aft* cages. Then, the HONNH species is generated, which are endothermic and exothermic for INT6′ and INT6, respectively. A high energy barrier is also found for the following formation of N_2 and H_2O, which are 155, 134, and 138 kJ mol^{-1} for the *gme*, *cha*, and *aft* cages. The bare Cu^I ion is formed after the desorption of N_2 and H_2O. The Cu^I ion is placed at the *8r* site in the energy profiles, which can migrate to the *d6r* site due to the higher stability (Fig. 2). Note that the observed high energy barriers are not surprising for the intramolecular proton transfer due to the formation of an unstable four-membered ring, as indicated in Fig. 3 and S2† (TS4 and TS4′). The so-called hydrogen push–pull mechanism has been proposed for the NH_2NO decomposition, which occurs at the Brønsted acid site with lower energy barriers.[15,35,54] We studied the NH_2NO decomposition at Brønsted acid site in the *gme* cage, which has lower reaction barriers (more details will follow in a subsequent section). Overall, the formation of NH_2NO needs to overcome high barriers for the three cages when the $[Cu^{II}(OH)]^+$ unit serves as the active site.

When the Cu^{II} ion is considered as the active site, the Cu^{II}-*cha*, -*gme*, and -*aft* models with two Si atoms separating the Al pair are applied. As presented in Scheme S1,† the formation of Cu^I–NH_2NO is accompanied by the generation of a Brønsted acid proton on the framework O, which can easily adsorb the second NH_3. Therefore, two NH_3 molecules are applied in this case. As shown in Fig. 4 and S3,† with the assistance of the second NH_3 molecule, the respective barriers for the Cu^I–NH_2NO formation are 70, 73, 63 kJ mol^{-1} for *cha*, *gme*, and *aft*, which are much lower compared to those on the $[Cu^{II}(OH)]^+$ active site. The following intramolecular H transfer still exhibits high energy barriers, that is, 172, 162, and 164 kJ mol^{-1} for *cha*, *gme*, and *aft*, respectively. However, when it comes to the following formation of N_2 and H_2O, the energy barriers are decreased to 89, 77, 81 kJ mol^{-1} for *cha*, *gme*, and *aft*, respectively, which should be ascribed to the stabilization of OH^- by the NH_3 molecule. Based on the results, the Cu^{II} ion at the *d6r* site is more favorable as the active site compared to the $[Cu^{II}(OH)]^+$ site, and the involvement of the second NH_3 molecule also facilitates the formation of NH_2NO.

To further study the influence of NH_3 on the formation of the NH_2NO species, four NH_3 molecules are adsorbed to the Cu^{II} active site forming the square planner $[Cu^{II}(NH_3)_4]^{2+}$ amino complex, which is a dominant species at low temperatures.[13] The formation of $[Cu^{II}(NH_3)_4]^{2+}$ are strongly exothermic, which exhibit similar adsorption energies of −494, −493, −489 kJ mol^{-1} for *cha*, *gme*, and *aft*, respectively. Fig. 5 shows energy profiles for the formation of NH_2NO. The adsorption of NO is exothermic, which have adsorption energies of −26, −23, and −32 kJ mol^{-1} for *cha*, *gme*, and *aft*, respectively. Upon the adsorption of NO, the resulting structures have the triplet ground state for the three frameworks, which are slightly more stable than the singlet

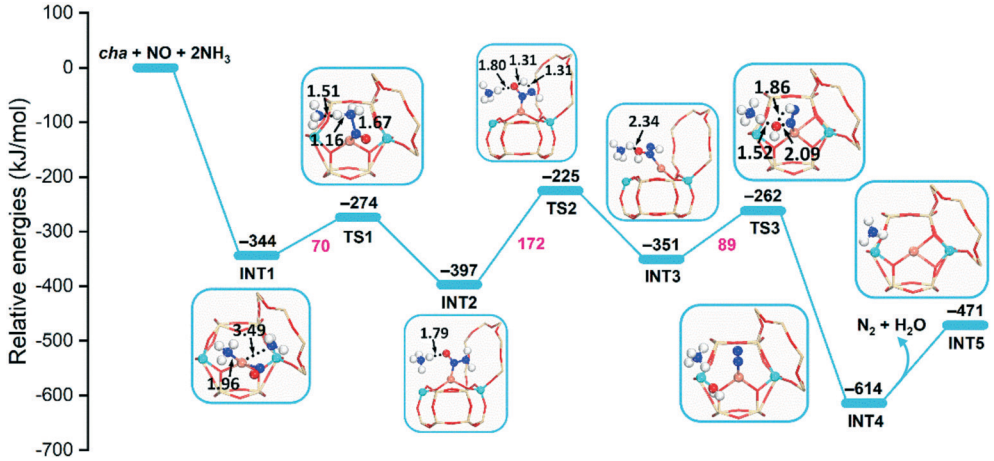

Fig. 4 Reaction energy diagrams and optimized structures of intermediates and transition states for reduction by NO and NH_3 on Cu^{II}–2Al-*cha*.

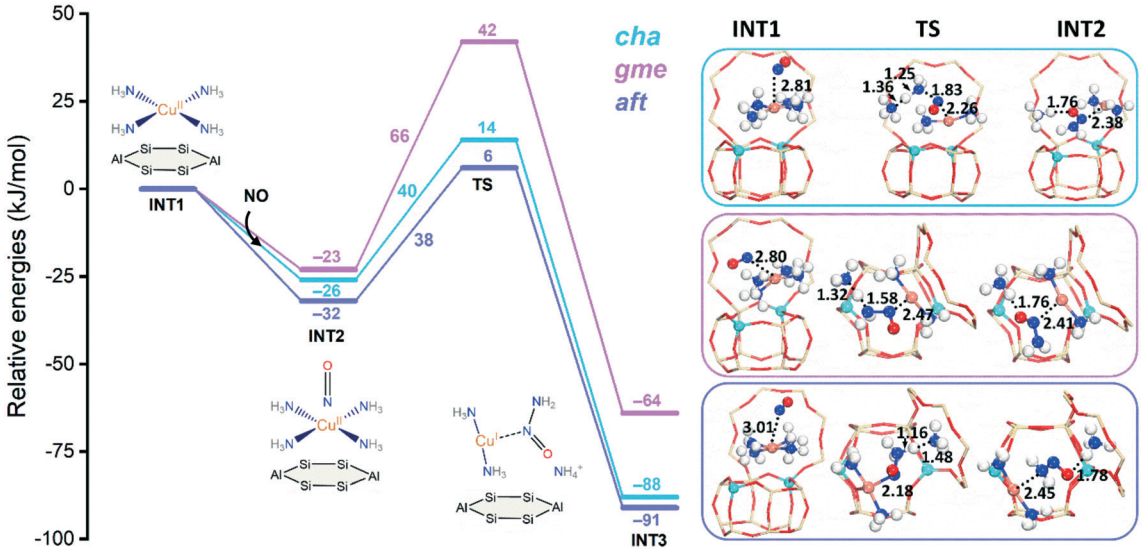

Fig. 5 Reaction energy diagrams and optimized structures of intermediates and transition states for reduction at the $[Cu^{II}(NH_3)_4]^{2+}$ site of Cu^{II}–2Al-*cha*, -*gme*, and *aft*.

state by 8, 2, and 8 kJ mol^{-1} for *cha*, *gme*, and *aft*, respectively. The following formation of NH_2NO is accompanied by the formation of the linear $[Cu^{I}(NH_3)_2]^{+}$ complex observed in experiments.[13] Furthermore, the observed energy barriers are 40 and 38 kJ mol^{-1} for *cha* and *aft*, which are much lower than those at the bare Cu^{II} site. However, the energy barrier of 66 kJ mol^{-1} in *gme* is only slightly lower than that at the bare Cu^{II} site, which should be attributed to the small inner space in *gme*. As summarized in Table S1,† the *gme* cage has the largest deformation energies than the other two cages. The deformation energy was calculated as the energy difference between the zeolite cage from INT/TS and the free zeolite cage. Therefore, because of the limited cage size, the NH_2NO formation at the $[Cu^{II}(NH_3)_4]^{2+}$ site is less preferred in the *gme* cage than the other two cages.

Fig. 6 compares reaction energy barriers for the NH_2NO formation at the $[Cu^{II}(OH)]^{+}$, Cu^{II}, and $[Cu^{II}(NH_3)_4]^{2+}$ sites in the three cages. The reaction between NO and NH_3 at $[Cu^{II}(OH)]^{+}$ has very high energy barriers in all cages, in which the *gme* and *aft* cages have slightly higher barriers. The lower barriers are found at the Cu^{II} site for the reaction between NO and $2NH_3$ molecules, and the similar barriers indicate small differences caused by the cage size. At the $[Cu^{II}(NH_3)_4]^{2+}$ site, upon adsorption of NO, the smallest *gme* cage has the highest energy barrier due to the largest deformation energies compared to the other two cages. Therefore, compared to $[Cu^{II}(OH)]^{+}$, the bare Cu^{II} site is more favorable for reduction, and the selectivity caused by cage size is not identified so much at the Cu^{II} site. For the NH_3-solvated $[Cu^{II}(NH_3)_4]^{2+}$ site at low temperatures, the smallest *gme* cage is not preferred.

As mentioned above, the intramolecular NH_2NO decomposition has high energy barriers due to the formation of an unstable four-membered ring in TS. The proton

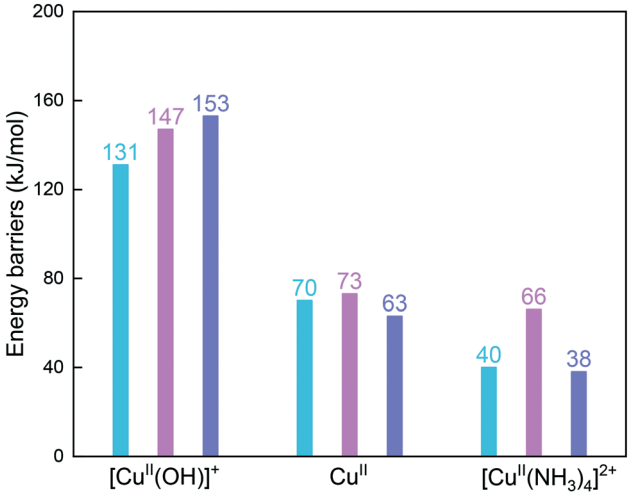

Fig. 6 Reaction energy barriers for the formation of NH_2NO at the $[Cu^{II}(OH)]^+$, Cu^{II}, and $[Cu^{II}(NH_3)_4]^{2+}$ sites for *cha* (blue), *gme* (pink), and *aft* (purple) cages (the energy barrier for the H_2O formation at $[Cu^{II}(OH)]^+$ is shown, which is the highest energy barrier during the NH_2NO formation).

exchange between NH_2NO and a Brønsted acid site can significantly reduce the reaction barriers, that is, the hydrogen push–pull mechanism, which has been explored in NH_3-SCR over V_2O_5 (ref. 54) and zeolites.[15,35] We examined the NH_2NO decomposition at the Brønsted acid site in the *gme* cage. As shown in Fig. 7, the adsorption of NH_2NO at Brønsted acid site is exothermic by −92 kJ mol^{-1}. In subsequent steps, the NH_2NO species adjusts its configurations by donating and receiving H, which eventually generates N_2 and H_2O. The observed reaction barriers are much lower than those obtained from the intramolecular NH_2NO decomposition. Therefore, the NH_2NO species will migrate to the Brønsted acid site to proceed the subsequent decomposition.

Oxidation in Cu-*cha*, Cu-*gme*, and Cu-*aft*

Fig. 8 presents the energy profiles for the NO oxidation in the Cu^I-*cha*, -*gme*, and -*aft* cages with one Al atom in the *d6r* site. The adsorption of NO and O_2 to the Cu^I ion is exothermic with adsorption energies of −154, −160, and −161 kJ mol^{-1} for *cha*, *gme*, and *aft*. Upon the adsorption, the O_2 molecule is activated through the weakening of the O–O bond, which is accompanied by the lengthening of the Cu–N bond. After moderate energy barriers of 55, 51, and 52 kJ mol^{-1} for *cha*, *gme*, and *aft*, one O atom of O_2 is transferred to the NO molecule. Subsequently, the nitrate (NO_3^-) is formed by transferring the other O atom of O_2 to the NO_2 unit with the energy barriers of 17, 19, and 20 kJ mol^{-1} for *cha*, *gme*, and *aft*, which is strongly exothermic. The species has a chelating bidentate nitrate configuration on a monomeric Cu ion, which has been confirmed by the Fourier transformed EXAFS spectra.[13] Overall, the similar energy barriers are observed for the formation of the nitrate in the three frameworks.

In the next step, the second NO molecule is adsorbed to the Cu ion with similar energetics of −370, −383, and −376 kJ mol^{-1} for *cha*, *gme*, and *aft*. Subsequently, one O atom of the nitrate is transferred to the NO molecule through energy barriers of 71, 93, and 68 kJ mol^{-1} for *cha*, *gme*, and *aft*, where the smallest *gme* cage has the highest barrier than the other two frameworks (also see Fig. 9). Analyses on the deformation energy of the zeolite cage revealed that the largest deformation energy of TS3 in the *gme* cage should contribute to the highest energy barrier (Table S2†). The resulting intermediates (INT5) are endothermic (−340, −330, and −341 kJ mol^{-1} for *cha*, *gme*, and *aft*) with respect to the former step, which is the same situation as the previous study of Cu-CHA.[13] Therefore, a higher energy barrier is found for the formation of nitrite than that for the nitrate formation, which is different from the previous study.[13]

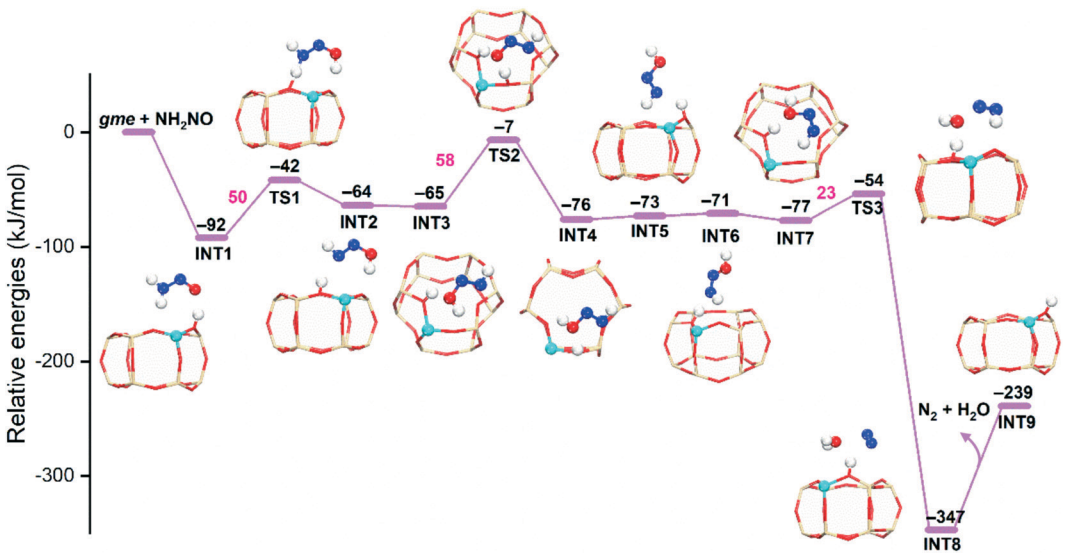

Fig. 7 Reaction energy diagrams and local structures of intermediates and transition states for NH_2NO decomposition assisted by Brønsted acid sites (AlH-*gme*).

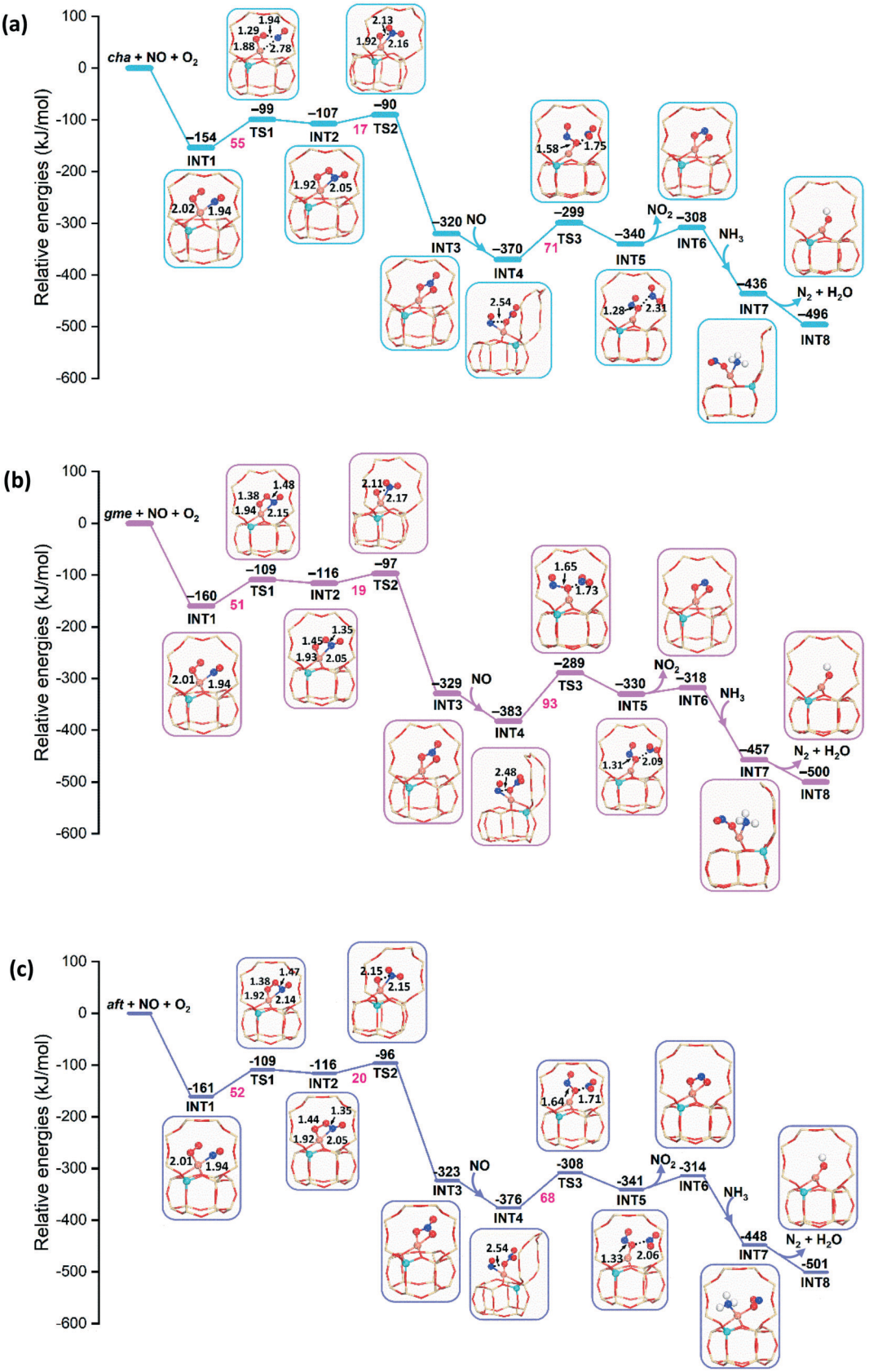

Fig. 8 Reaction energy diagrams and local geometries of intermediates and transition states for the oxidation by NO and O_2 on Cu^I–Al-*cha* (a), -*gme* (b), and -*aft* (c).

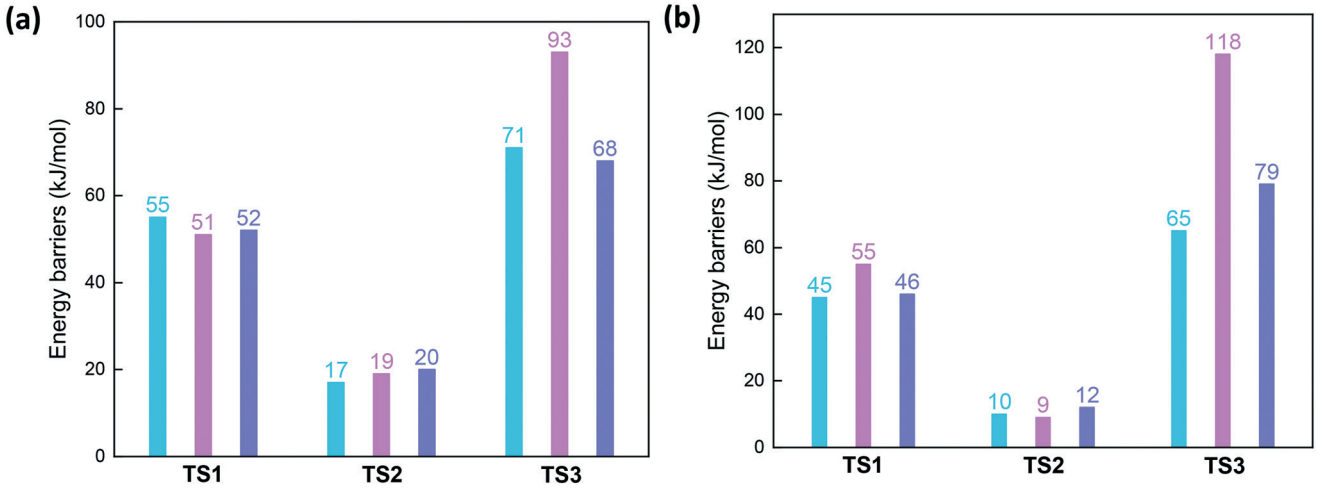

Fig. 9 Reaction barriers of three transition states during oxidation by NO and O_2 on Cu^I–Al-*cha*, -*gme*, and -*aft* (a) as well as Cu^I–2AlH-*cha*, -*gme*, and -*aft* (b).

Interestingly, the calculated energy barrier of 71 kJ mol^{-1} is very close to the apparent activation energy of 69 kJ mol^{-1} for the oxidation on Cu-CHA.[13] Overall, as summarized in Fig. 9a, the highest energy barrier is observed for TS3 during the oxidation in all three types of frameworks, especially, the smallest *gme* cage possesses the highest energy barrier. Then, the aadsorption of NH_3 to the Cu ion are strongly exothermic, and the adsorption energies are −436, −457, and −448 kJ mol^{-1} for *cha*, *gme*, and *aft*, respectively. The reaction pathway for the formation of H_2O and N_2 is still unclear, therefore, only the energetics of INT8 relative to INT7, H_2O and N_2 are shown in energy profiles.

The models with two Al atoms accompanied by one Brønsted acid site are also considered for the oxidation process, which can simulate the oxidation of catalyst with acidic properties. As shown in Fig. S4,† the adsorption energies of NO and O_2 are −142, −154, and −139 kJ mol^{-1} for *cha*, *gme*, and *aft*, which are smaller compared to those on the 1Al site. Meanwhile, it is found that energy barriers for the first O transfer in the *cha* and *aft* cages are slightly decreased to 45 and 46 kJ mol^{-1}, while that in the *gme* cage is slightly increased to 55 kJ mol^{-1} due to the more stable complex adsorbing NO and O_2. The next energy barriers for the formation of nitrate are decreased to 10, 9, and 12 kJ mol^{-1} for *cha*, *gme*, and *aft*, which should be partially ascribed to the formation of the hydrogen bonds (Fig. S5†). Note that the energetics of INT1, TS1, INT2, and TS2 on the 2Al site are less stable than those on the 1Al site for *aft*, while the other two frameworks have comparable values on 1Al and 2Al sites. The deformation energy of INT2 on *aft* is 163 kJ mol^{-1}, which is even larger than those on *cha* (147 kJ mol^{-1}) and *gme* (150 kJ mol^{-1}) (Table S3†). The formation of the nitrate species possesses similar reaction energies to those on 1Al site, that is, −321, −332, and −319 kJ mol^{-1} for *cha*, *gme*, and *aft*.

After the second NO molecule is adsorbed, the O transfer from the nitrate to the NO has the energy barriers of 65, 118, and 79 kJ mol^{-1} for *cha*, *gme*, and *aft* (Fig. 9b and S4†), in which *gme* and *aft* exhibit higher barriers than those on the 1Al site. As shown in Fig. 10, the INT4a and INT4b are considered to represent the different positions of the adsorbed molecules relative to the Brønsted proton. The INT4a structures are more stable due to the hydrogen bond interaction. The INT4b configurations are shown in the energy profiles due to the resulting lower barriers. It is also found that the energy difference of INT4a and INT4b increases with the increasing cage size, that is, 7, 12, and 23 kJ mol^{-1} for *gme*, *cha*, and *aft*, respectively. The energetics of the located TS3 structures are −280, −312, and −284 kJ mol^{-1} for *gme*, *cha*, and *aft*, thus, the highest energy barrier of 118 kJ mol^{-1} is observed on the *gme* cage (Fig. S4†). Fig. S6† also

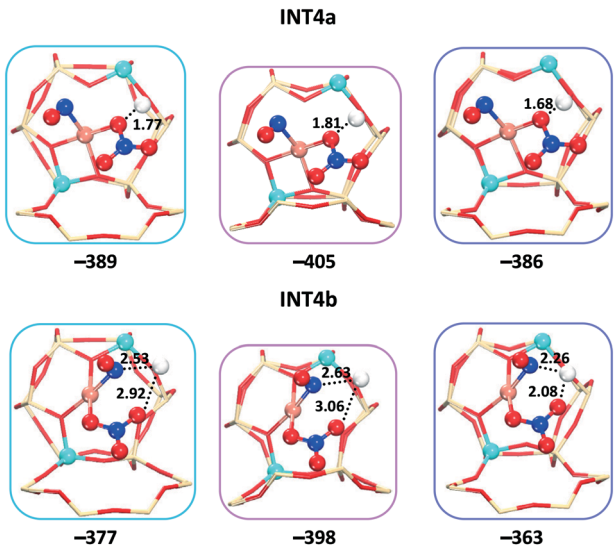

Fig. 10 Local geometries of the two intermediates (INT4a and INT4b) on *cha* (blue), *gme* (pink), and *aft* (purple). The distances between the adsorbed molecules and the Brønsted proton are shown in angstrom. The values beneath each structure are reaction energies with respect to the isolated reactants.

shows the distances between the adsorbed molecules and the Brønsted proton in INT5 and INT6. When an NH_3 molecule is introduced, the reaction energies are −503, −505, and −490 kJ mol^{-1} for *cha*, *gme*, and *aft*, which are more exothermic due to the formation of NH_4^+ at the Brønsted acid site. Then, the NH_4NO_2 species can be formed, which can be easily decomposed into N_2 and H_2O under SCR operation conditions.[55–57] Therefore, the results on the 2Al site still reveal that the oxidation process on the *gme* cage needs the largest activation energy compared to the *cha* and *aft* cages (Fig. 9b). The results on the bare Cu^{II} ions will be useful for the high temperature oxidation.

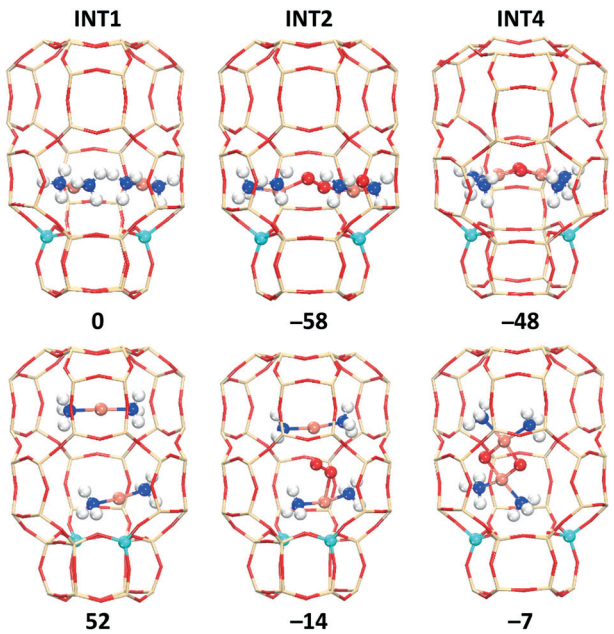

Fig. 11 Optimized structures and relative energies (kJ mol^{-1}) of INT1, INT2, and INT4 for the *cha* cage (top: para-site; bottom: per-site). The energies of INT2 and INT4 are obtained with respect to the para-site INT1 and O_2.

We also evaluated the O_2 activation by paring of $[Cu^I(NH_3)_2]^+$ in the *cha*, *aft*, and *gme* cages, which is an important step for the low temperature oxidation with low Cu loadings. Due to the large inner space in the *cha* and *aft* cages, the two $[Cu^I(NH_3)_2]^+$ species inside these cages may have two different alignments with respect to the *d6r*: parallel to the *d6r* (para-site) and perpendicular to the *d6r* (per-site). Fig. 11 and S8† show the two different alignments for INT1, INT2, and INT4 in *cha* and *aft*. The *gme* cage can only have the $[Cu^I(NH_3)_2]^+$ pair at the para-site due to the restricted space, as shown in Fig. S7.† Note that previous studies only considered the per-site to place the two $[Cu^I(NH_3)_2]^+$ species.[35,58] It is found that the INT1 structures with the per-site are over 50 kJ mol^{-1} higher in energy compared to those with the para-site. The following INT2 and INT4 structures also have the same preference for the para-site. In order to explain the stabilization of the inner species at the para-site, we calculated the interaction energies between the inner species and the outer cages of INT1 and INT4. As shown in Table S4,† the separated fragments (the outer cage and the inner species) from the per-site structures are more stable than those from the para-site ones, however, stronger interaction energies between the two fragments were identified for the para-site case. Therefore, the higher stability of the para-site structures originates from the stronger interactions between the inner species and the outer cages.

Fig. 12 shows energy profiles of the O_2 activation for *cha*, *aft*, and *gme*, in which the para-site structures are shown. The O_2 insertion is the most favorable in the largest *aft* cage (−67 kJ mol^{-1}), followed by the *cha* cage (−58 kJ mol^{-1}), while the corresponding energy is only −17 kJ mol^{-1} in the smallest *gme* cage. The following INT3 also follows the same sequence in reaction energy, *aft* > *cha* > *gme*. Fig. S10† shows the

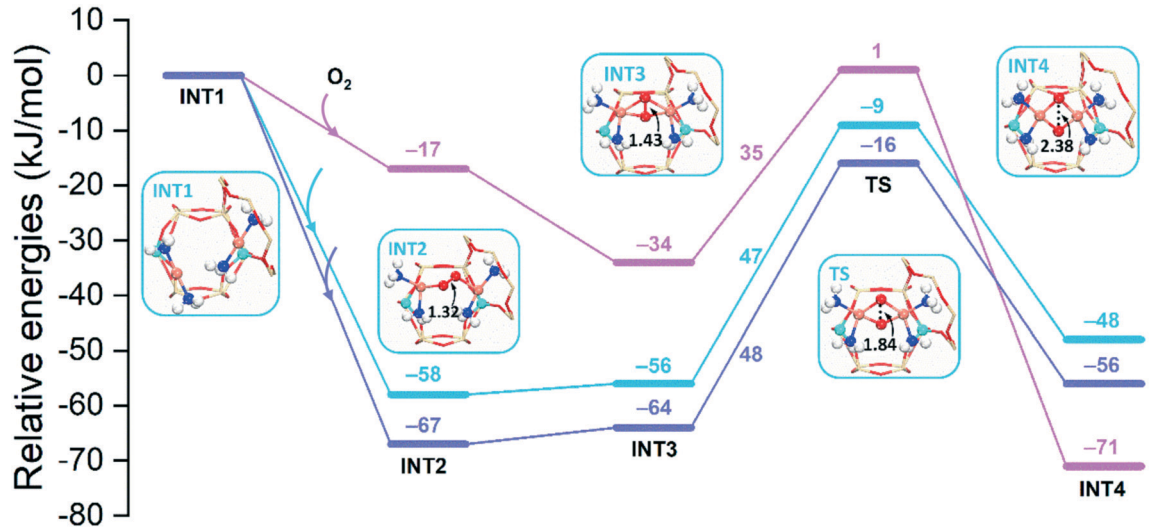

Fig. 12 Reaction energy diagrams for the O_2 activation by the 2[NH_3–Cu^I–NH_3] dimer in 2Al-*cha* (blue), -*gme* (pink), and -*aft* (purple). Local geometries of intermediates and transition states for *cha* are shown.

potential energy surface between INT2 and INT3 for the *cha* cage because the corresponding TS search fails. Interestingly, a new intermediate with a lower energy than INT2 is identified along the potential energy surface, in which the O–O distance is in the range of 1.36–1.38 Å. Meanwhile, it is found that the significant energy barrier between INT2 and INT3 does not exist and the spin-crossing occurs *via* minimum energy seam of crossing (MESX) in the vicinity of INT3 as shown in Fig. S10.† As for the transition state between INT3 and INT4, reaction barriers are almost the same for *cha* (47 kJ mol^{-1}) and *aft* (48 kJ mol^{-1}), while a lower barrier is found in *gme* (35 kJ mol^{-1}). Note that the TS in *gme* is the most unstable one, and the lower barrier in *gme* should be partially ascribed to the lower stability of INT3. The resulting INT4 is the most exothermic in *gme* (−71 kJ mol^{-1}), followed by *aft* (−56 kJ mol^{-1}) and *cha* (−48 kJ mol^{-1}). The most exothermic INT4 in *gme* should be due to the strongest interaction than *cha* and *aft* (Table S4†). Even though the *gme* cage has the largest reaction energy for the INT4 formation, the smallest adsorption energy (INT2) in *gme* suggests the encapsulation of O_2 into the small cage is more difficult compared to the other two cages, which can inhibit the process to proceed. In general, it can be concluded that the *aft* cage has the similar activity for the O_2 activation to the *cha* cage.

As for all intermediates and transition states, natural electron configurations and natural population analysis (NPA) partial charges of Cu are summarized in ESI† (Tables S5–S10 and Fig. S11–S13). The results revealed that the electrons from the 3d orbital have more significant changes than those from the 4s orbital when the oxidation state of Cu changes during the reaction.

Conclusions

By means of DFT calculations, the SCR activity in the Cu-exchanged CHA, GME, and AFX zeolites are evaluated through the Cu-*cha*, -*gme*, and -*aft* cages, and the oxidation and reduction processes are both studied. We considered Cu^{I}, Cu^{II}, and $[Cu^{II}(OH)]^{+}$ as the active sites which are placed in the frameworks with the 1Al or 2Al site. As for the reduction process, the $[Cu^{II}(OH)]^{+}$ (1Al) and the Cu^{II} (2Al) are constructed to proceed the reaction. The results have revealed that the NH_2NO formation at the $[Cu^{II}(OH)]^{+}$ site has high energy barriers in the three considered frameworks, while the lower barriers are found at the Cu^{II} site for them. Additionally, the barriers are largely decreased at the solvated $[Cu^{II}(NH_3)_4]^{2+}$ site for the *cha* and *aft* frameworks, while the barrier is only slightly decreased for *gme*. The formed NH_2NO species then migrates to the Brønsted acid site for the formation of N_2 and H_2O. The Cu^{I} (1Al) and the Cu^{I} plus a Brønsted acid site (2Al) are constructed to study the oxidation process. The results on both models have revealed that the nitrate formation has similar energy barriers in the three frameworks, which are lower than the following nitrite formation. Particularly, the smallest *gme* cage possesses the highest energy barrier for the nitrite formation, which should be ascribed to the largest deformation caused by the limited space. It is also found that the Brønsted acid proton can slightly affect the stability of the intermediates and transition states, which has little influence on the general trend. As for the O_2 activation by paring of $[Cu^{I}(NH_3)_2]^{+}$, *cha* and *aft* have similar performance, whereas *gme* is not favorable due to the limited space for the insertion of O_2. Overall, the reactivity differences in the three cages have revealed the cage size is important to proceed this reaction, which may provide a way to tune the reaction pathway by the cage size selectivity. Additionally, it can be concluded that the AFX zeolite has the comparable SCR catalytic activity to the CHA one, even though further studies are demanded.

Conflicts of interest

The authors declare no competing financial interest.

Acknowledgements

This work was supported by the Research Association of Automotive Internal Combustion Engines (AICE) project, Japan. M. E. acknowledges Grants from Japan Society for the Promotion of Science (Grant numbers of JP16H06511, JP20H02718).

References

1 R. M. Barrer, *Zeolites*, 1981, **1**, 130–140.
2 M. Iwamoto and H. Hamada, *Catal. Today*, 1991, **10**, 57–71.
3 G. Centi and S. Perathoner, *Appl. Catal., A*, 1995, **132**, 179–259.
4 B. Chen, R. Xu, R. Zhang and N. Liu, *Environ. Sci. Technol.*, 2014, **48**, 13909–13916.
5 J. H. Kwak, R. G. Tonkyn, D. H. Kim, J. Szanyi and C. H. F. Peden, *J. Catal.*, 2010, **275**, 187–190.
6 E. Borfecchia, P. Beato, S. Svelle, U. Olsbye, C. Lamberti and S. Bordiga, *Chem. Soc. Rev.*, 2018, **47**, 8097–8133.
7 M. Dusselier and M. E. Davis, *Chem. Rev.*, 2018, **118**, 5265–5329.
8 Y. Xin, Q. Li and Z. Zhang, *ChemCatChem*, 2018, **10**, 29–41.
9 F. Gao, E. D. Walter, E. M. Karp, J. Luo, R. G. Tonkyn, J. H. Kwak, J. Szanyi and C. H. F. Peden, *J. Catal.*, 2013, **300**, 20–29.
10 F. Gao, E. D. Walter, M. Kollar, Y. Wang, J. Szanyi and C. H. F. Peden, *J. Catal.*, 2014, **319**, 1–14.
11 S. A. Bates, A. A. Verma, C. Paolucci, A. A. Parekh, T. Anggara, A. Yezerets, W. F. Schneider, J. T. Miller, W. N. Delgass and F. H. Ribeiro, *J. Catal.*, 2014, **312**, 87–97.
12 C. Paolucci, A. A. Verma, S. A. Bates, V. F. Kispersky, J. T. Miller, R. Gounder, W. N. Delgass, F. H. Ribeiro and W. F. Schneider, *Angew. Chem., Int. Ed.*, 2014, **53**, 11828–11833.
13 T. V. W. Janssens, H. Falsig, L. F. Lundegaard, P. N. R. Vennestrøm, S. B. Rasmussen, P. G. Moses, F. Giordanino, E. Borfecchia, K. A. Lomachenko, C. Lamberti, S. Bordiga, A. Godiksen, S. Mossin and P. Beato, *ACS Catal.*, 2015, **5**, 2832–2845.

14 C. Paolucci, A. A. Parekh, I. Khurana, J. R. Di Iorio, H. Li, J. D. Albarracin Caballero, A. J. Shih, T. Anggara, W. N. Delgass, J. T. Miller, F. H. Ribeiro, R. Gounder and W. F. Schneider, *J. Am. Chem. Soc.*, 2016, **138**, 6028–6048.
15 Y. Mao, Z. Wang, H.-F. Wang and P. Hu, *ACS Catal.*, 2016, **6**, 7882–7891.
16 F. Gao, D. Mei, Y. Wang, J. Szanyi and C. H. F. Peden, *J. Am. Chem. Soc.*, 2017, **139**, 4935–4942.
17 M. Moreno-González, R. Millán, P. Concepción, T. Blasco and M. Boronat, *ACS Catal.*, 2019, **9**, 2725–2738.
18 L. S. Dent and J. V. Smith, *Nature*, 1958, **181**, 1794–1796.
19 R. F. Lobo, S. I. Zones and R. C. Medrud, *Chem. Mater.*, 1996, **8**, 2409–2411.
20 S. V. Priya, T. Ohnishi, Y. Shimada, Y. Kubota, T. Masuda, Y. Nakasaka, M. Matsukata, K. Itabashi, T. Okubo, T. Sano, N. Tsunoji, T. Yokoi and M. Ogura, *Bull. Chem. Soc. Jpn.*, 2017, **91**, 355–361.
21 A. H. Clark, R. J. G. Nuguid, P. Steiger, A. Marberger, A. W. Petrov, D. Ferri, M. Nachtegaal and O. Kröcher, *ChemCatChem*, 2020, **12**, 1429–1435.
22 N. Martín, C. Paris, P. N. R. Vennestrøm, J. R. Thøgersen, M. Moliner and A. Corma, *Appl. Catal., B*, 2017, **217**, 125–136.
23 H. Kubota, C. Liu, T. Toyao, Z. Maeno, M. Ogura, N. Nakazawa, S. Inagaki, Y. Kubota and K.-i. Shimizu, *ACS Catal.*, 2020, **10**, 2334–2344.
24 E. Borfecchia, K. A. Lomachenko, F. Giordanino, H. Falsig, P. Beato, A. V. Soldatov, S. Bordiga and C. Lamberti, *Chem. Sci.*, 2015, **6**, 548–563.
25 A. Godiksen, F. N. Stappen, P. N. R. Vennestrøm, F. Giordanino, S. B. Rasmussen, L. F. Lundegaard and S. Mossin, *J. Phys. Chem. C*, 2014, **118**, 23126–23138.
26 U. Deka, I. Lezcano-Gonzalez, B. M. Weckhuysen and A. M. Beale, *ACS Catal.*, 2013, **3**, 413–427.
27 J. Szanyi, J. H. Kwak, H. Zhu and C. H. F. Peden, *Phys. Chem. Chem. Phys.*, 2013, **15**, 2368–2380.
28 F. Giordanino, E. Borfecchia, K. A. Lomachenko, A. Lazzarini, G. Agostini, E. Gallo, A. V. Soldatov, P. Beato, S. Bordiga and C. Lamberti, *J. Phys. Chem. Lett.*, 2014, **5**, 1552–1559.
29 C. Paolucci, I. Khurana, A. A. Parekh, S. Li, A. J. Shih, H. Li, J. R. Di Iorio, J. D. Albarracin-Caballero, A. Yezerets, J. T. Miller, W. N. Delgass, F. H. Ribeiro, W. F. Schneider and R. Gounder, *Science*, 2017, **357**, 898–903.
30 K. A. Lomachenko, E. Borfecchia, C. Negri, G. Berlier, C. Lamberti, P. Beato, H. Falsig and S. Bordiga, *J. Am. Chem. Soc.*, 2016, **138**, 12025–12028.
31 A. Marberger, A. W. Petrov, P. Steiger, M. Elsener, O. Kröcher, M. Nachtegaal and D. Ferri, *Nat. Catal.*, 2018, **1**, 221–227.
32 F. Giordanino, E. Borfecchia, K. A. Lomachenko, A. Lazzarini, G. Agostini, E. Gallo, A. V. Soldatov, P. Beato, S. Bordiga and C. Lamberti, *J. Phys. Chem. Lett.*, 2014, **5**, 1552–1559.
33 E. Borfecchia, C. Negri, K. A. Lomachenko, C. Lamberti, T. V. W. Janssens and G. Berlier, *React. Chem. Eng.*, 2019, **4**, 1067–1080.
34 C. Negri, E. Borfecchia, M. Cutini, K. A. Lomachenko, T. V. W. Janssens, G. Berlier and S. Bordiga, *ChemCatChem*, 2019, **11**, 3828–3838.
35 L. Chen, T. V. W. Janssens, P. N. R. Vennestrøm, J. Jansson, M. Skoglundh and H. Grönbeck, *ACS Catal.*, 2020, **10**, 5646–5656.
36 F. Göltl, P. Sautet and I. Hermans, *Catal. Today*, 2016, **267**, 41–46.
37 J. S. McEwen, T. Anggara, W. F. Schneider, V. F. Kispersky, J. T. Miller, W. N. Delgass and F. H. Ribeiro, *Catal. Today*, 2012, **184**, 129–144.
38 F. Göltl, R. E. Bulo, J. Hafner and P. Sautet, *J. Phys. Chem. Lett.*, 2013, **4**, 2244–2249.
39 F. Göltl and J. Hafner, *J. Chem. Phys.*, 2012, **136**, 064501.
40 U. Deka, A. Juhin, E. A. Eilertsen, H. Emerich, M. A. Green, S. T. Korhonen, B. M. Weckhuysen and A. M. Beale, *J. Phys. Chem. C*, 2012, **116**, 4809–4818.
41 R. Zhang, J.-S. McEwen, M. Kollár, F. Gao, Y. Wang, J. Szanyi and C. H. F. Peden, *ACS Catal.*, 2014, **4**, 4093–4105.
42 Y. Zhao and D. G. Truhlar, *J. Chem. Phys.*, 2006, **125**, 194101.
43 C. Kumsapaya, K. Bobuatong, P. Khongpracha, Y. Tantirungrotechai and J. Limtrakul, *J. Phys. Chem. C*, 2009, **113**, 16128–16137.
44 Y. Zhao and D. G. Truhlar, *J. Phys. Chem. C*, 2008, **112**, 6860–6868.
45 P. Zhao, B. Boekfa, T. Nishitoba, N. Tsunoji, T. Sano, T. Yokoi, M. Ogura and M. Ehara, *Microporous Mesoporous Mater.*, 2020, **294**, 109908.
46 T. J. Goncalves, P. N. Plessow and F. Studt, *ChemCatChem*, 2019, **11**, 4368–4376.
47 M. M. Francl, W. J. Pietro, W. J. Hehre, J. S. Binkley, M. S. Gordon, D. J. DeFrees and J. A. Pople, *J. Chem. Phys.*, 1982, **77**, 3654–3665.
48 W. J. Hehre, R. Ditchfield and J. A. Pople, *J. Chem. Phys.*, 1972, **56**, 2257–2261.
49 M. Dolg, U. Wedig, H. Stoll and H. Preuss, *J. Chem. Phys.*, 1987, **86**, 866–872.
50 M. J. Frisch, G. W. Trucks, H. B. Schlegel, G. E. Scuseria, M. A. Robb, J. R. Cheeseman, G. Scalmani, V. Barone, B. Mennucci and G. A. Petersson *et al.*, *Gaussian 09, Revision E.01*, Gaussian, Inc, Wallingford Ct, 2013.
51 J. Rudolph and C. R. Jacob, *ACS Omega*, 2019, **4**, 7987–7993.
52 C. Prestipino, G. Berlier, F. X. Llabrés i Xamena, G. Spoto, S. Bordiga, A. Zecchina, G. Turnes Palomino, T. Yamamoto and C. Lamberti, *Chem. Phys. Lett.*, 2002, **363**, 389–396.
53 F. X. Llabrés i Xamena, P. Fisicaro, G. Berlier, A. Zecchina, G. T. Palomino, C. Prestipino, S. Bordiga, E. Giamello and C. Lamberti, *J. Phys. Chem. B*, 2003, **107**, 7036–7044.
54 M. Anstrom, N.-Y. Topsøe and J. A. Dumesic, *J. Catal.*, 2003, **213**, 115–125.
55 F. Liu, Y. Yu and H. He, *Chem. Commun.*, 2014, **50**, 8445–8463.
56 A. M. Beale, F. Gao, I. Lezcano-Gonzalez, C. H. F. Peden and J. Szanyi, *Chem. Soc. Rev.*, 2015, **44**, 7371–7405.
57 L. Ma, Y. Cheng, G. Cavataio, R. W. McCabe, L. Fu and J. Li, *Appl. Catal., B*, 2014, **156–157**, 428–437.
58 C. Liu, H. Kubota, T. Toyao, Z. Maeno and K.-i. Shimizu, *Catal. Sci. Technol.*, 2020, **10**, 3586–3593.

